



## Modeling Polymer Electrolyte Fuel Cells with Large Density and Velocity Changes

Yun Wang and Chao-Yang Wang<sup>\*,z</sup>

Electrochemical Engine Center and Department of Mechanical and Nuclear Engineering, The Pennsylvania State University, University Park, Pennsylvania 16802, USA

A model fully coupling the flow, species transport, and electrochemical kinetics in polymer electrolyte fuel cells is presented to explore operation undergoing very large density and velocity variations. Comparisons are also made to a previous constant-flow model, which neglects the mass source/sink from the continuity equation and assumes constant gas density. Numerical results reveal large density (>50%) and velocity (>80%) variations occurring in the anode at anode stoichiometry of 1.2. In addition, the hydrogen concentration remained as high as the inlet owing to deceleration of the anode gas flow. Finally, the constant-flow model is accurate within 14% under common operating conditions, *i.e.*, for anode stoichiometry ranging from 1.2 to 2.0.  
© 2005 The Electrochemical Society. [DOI: 10.1149/1.1851059] All rights reserved.

Manuscript submitted June 9, 2004; revised manuscript received August 2, 2004. Available electronically January 12, 2005.

Mathematical modeling of polymer electrolyte fuel cells (PEFCs) has been a rapidly growing field of research.<sup>1</sup> Grossly, previous models may be categorized into three groups. The first group,<sup>2-6</sup> mostly earlier work, focused on electrochemical modeling in one or pseudo-two dimensions. Gas flow and density along anode and cathode channels were either ignored or assumed to remain constant and uniform throughout a PEFC.

The second group was based primarily on the computational fluid dynamics (CFD) approach, where two- or three-dimensional solutions were obtained by solving transport equations governing conservation of mass, momentum, species, energy, and charge. The multidimensional flow fields in anode and cathode gas channels were solved independently and provided as an input to the species and energy equations. This group of models recognized that, under normal operating conditions, flow and density fields in gas channels remain approximately invariable. Thus, a simplification was made to neglect the mass source/sink term in the continuity equation and assume a constant gas density in the momentum equation. This yielded decoupling of the flow field from the species, electric potential, and temperature fields, thereby significantly accelerating the calculations. Possible inaccuracy introduced by this splitting of the problem may occur on the anode side; however, the hydrogen concentration profile is relatively unimportant as the anode overpotential is typically negligible. In addition to reducing memory and computational requirements, this splitting of the fuel cell problem has the added advantage of allowing for the consideration of different cell voltages/current densities for the same flow field. Notable work in this category is the single-phase models proposed by Garau *et al.*<sup>7</sup> and Wang and co-workers.<sup>8-11</sup> These models included a detailed description of water and proton cotransport as well as electrochemical reactions in the membrane electrode assembly (MEA). Further, the model of Um *et al.*<sup>8-10,12</sup> has been successfully applied to large-scale simulations using parallel computing<sup>13</sup> as well as to the study of complex flow and transport phenomena in a 50 cm<sup>2</sup> PEFC.<sup>14</sup>

The decoupling of flow field from the species concentration field becomes impossible in PEFCs operated with large density and velocity variations, *e.g.*, under ultralow anode stoichiometry. Simulation of such extreme conditions calls for the third group of models where the gas flow field is fully coupled with electrochemical and transport equations. A representative work in this category is due to Dutta *et al.*<sup>15,16</sup> who proposed a model considering variable gas density and mass source/sink in the continuity equation. Unfortunately, all simulations in Ref. 15 and 16 were shown for cases with small density variation (less than 15%) along the channel. In addition, the velocity variation along the channel may affect the water distribution by convection, thus influencing cell performance especially un-

der low-humidity operation. Accurate capturing of water transport and distribution in PEFCs also requires a detailed MEA model, which was absent in the work of Dutta *et al.*<sup>15,16</sup> Büchi and Scherer<sup>17</sup> experimentally showed a strongly nonlinear water content profile prevailing in the Nafion membrane, and Kulikovskiy<sup>18</sup> numerically demonstrated the paramount importance of accounting for nonlinear water transport through the membrane. Meng and Wang<sup>13</sup> further pointed out that ohmic and transport losses in the catalyst layer are significant, especially for MEAs with thinner membranes, such that the catalyst layer cannot be treated as an interface without thickness. Most recently, Wang and Wang<sup>19</sup> indicated that water accumulation in a membrane of finite thickness controls the transient response of a PEFC.

The objective of this work is twofold. One is to expand upon the single-phase model of Um *et al.*<sup>8-10</sup> by including variable density and mass source/sink term in the continuity equation. This variable-flow model then fully couples flow, transport, and electrochemical processes as well as including a detailed MEA model. Our focus here is to apply this comprehensive model to explore PEFC behaviors under very large density (>50%) and velocity variations (>80%). Second, we compare the present full model with the previous constant-flow model to ascertain the validity range of the latter.

### Physical and Numerical Model

The fuel cell to be modeled includes the following subregions: the gas channels, gas-diffusion layers (GDLs), and catalyst layers in the anode and cathode sides, and membrane in the middle. Fuel and oxidant are conveyed by channel flows and distributed onto the anode and cathode. Reactants pass through the respective GDLs and reach the catalyst layers where electrochemical reactions occur. The membrane plays the dual role of a gas separator and an electrolyte, dividing the fuel and oxidant flows, and acting as the proton-conducting medium. In addition, the membrane allows water transport by diffusion and electro-osmotic drag so that there is a mass exchange of water through the membrane between the two gas streams.

A steady-state, isothermal model of PEFCs consists of four principles of conservation: mass, momentum, species, and charge<sup>8-10</sup>

$$\text{Continuity } \nabla \cdot (\rho \mathbf{u}) = S_m \quad [1]$$

$$\text{Momentum } \frac{1}{\epsilon^2} \nabla \cdot (\rho \mathbf{u} \mathbf{u}) = -\nabla p + \nabla \cdot \boldsymbol{\tau} + S_u \quad [2]$$

$$\text{Species } \nabla \cdot (\mathbf{u} C_k) = \nabla \cdot (D_k^{\text{eff}} \nabla C_k) + S_k \quad [3]$$

$$\text{Charge } 0 = \nabla \cdot (\kappa^{\text{eff}} \nabla \Phi_e) + S_\Phi \quad [4]$$

\* Electrochemical Society Active Member.

<sup>z</sup> E-mail: cxw31@psu.edu

**Table I. Physical and transport properties.**

Quantity	Value
Water saturation pressure, <sup>3</sup> $p^{\text{sat}}$ (Pa)	$\log_{10} p^{\text{sat}} = -2.1794 + 0.02953(T - 273.15) - 9.1837 \times 10^{-5}(T - 273.15)^2 + 1.4454 \times 10^{-7}(T - 273.15)^3$
Water activity, <sup>3</sup> $a$	$a = \frac{C_w RT}{p^{\text{sat}}}$
Membrane water content, <sup>3</sup> $\lambda$ ( $\text{H}_2\text{O}/\text{SO}_3^-$ )	$\lambda = \begin{cases} 0.043 + 17.81a - 39.85a^2 + 36.0a^3 & \text{for } 0 < a \leq 1 \\ 14 + 1.4(a - 1) & \text{for } 1 \leq a \leq 3 \end{cases}$
Ionic conductivity of membrane, <sup>3</sup> $\kappa$ (S/cm)	$(0.005139\lambda - 0.00326)\exp\left[1268\left(\frac{1}{303} - \frac{1}{T}\right)\right]$
$\text{H}_2\text{O}$ diffusivity in membrane, <sup>22</sup> $D_w^m$ ( $\text{cm}^2/\text{s}$ )	$D_w^m = \begin{cases} 3.1 \times 10^{-3}\lambda(e^{0.28\lambda} - 1) \cdot e^{[-2346/T]} & \text{for } 0 < \lambda \leq 3 \\ 4.17 \times 10^{-4}\lambda(1 + 161e^{-\lambda}) \cdot e^{[-2346/T]} & \text{otherwise} \end{cases}$
Electro-osmosis coefficient, <sup>23</sup> $n_d$ ( $\text{H}_2\text{O}/\text{H}^+$ )	$n_d = \begin{cases} 1.0 & \text{for } \lambda \leq 14 \\ \frac{1.5}{8}(\lambda - 14) + 1.0 & \text{otherwise} \end{cases}$
Membrane density, <sup>24</sup> $\rho$ ( $\text{kg}/\text{m}^3$ )	$\rho = \frac{1.98 + 0.0324\lambda}{1 + 0.0648\lambda} \times 10^3$
$\text{O}_2$ diffusivity in the membrane, <sup>2</sup> $D_{\text{O}_2}^m$ ( $\text{cm}^2/\text{s}$ )	$1.22 \times 10^{-6}$
Gas diffusion coefficient in porous media, $D^{\text{eff}}$ ( $\text{cm}^2/\text{s}$ )	$D^{\text{eff}} = \epsilon^{1.5}D$
Diffusivity in the gas channels, <sup>25</sup> $D$ ( $\text{m}^2/\text{s}$ )	$D_o\left(\frac{T}{353}\right)^{3/2}\left(\frac{1}{p}\right)$
$\text{H}_2/\text{H}_2\text{O}$ diffusivity in anode gas at standard condition, $D_{o,\text{H}_2,\text{a}}/D_{o,\text{w},\text{a}}$ ( $\text{m}^2/\text{s}$ )	$1.1028 \times 10^{-4}/1.1028 \times 10^{-4}$
$\text{O}_2/\text{H}_2\text{O}$ diffusivity in cathode gas at standard condition, $D_{o,\text{O}_2,\text{c}}/D_{o,\text{w},\text{c}}$ ( $\text{m}^2/\text{s}$ )	$3.2348 \times 10^{-5}/7.35 \times 10^{-5}$
Viscosity of anode/cathode gas, <sup>26</sup> $\mu$ ( $\text{kg}/\text{m s}$ )	$\mu = 9.88 \times 10^{-6}X_{\text{H}_2} + 1.12 \times 10^{-5}X_{\text{H}_2\text{O}} + 2.01 \times 10^{-5}X_{\text{N}_2} + 2.3 \times 10^{-5}X_{\text{O}_2}$

where  $\mathbf{u}$  is the superficial velocity in the porous media and the variable mixture density may be expressed as the function of molar concentrations of the components

$$\rho = \sum_k C_k M_k \quad [5]$$

The continuity equation for the gas mixture, Eq. 1, also may be obtained by summing up all species equations. That is, performing operation of  $\sum_k (M_k \times \text{Eq.3})$  yields

$$\nabla \cdot \left( \mathbf{u} \sum_k C_k M_k \right) = \nabla \cdot \left( \sum_k D_k^{\text{eff}} \nabla M_k C_k \right) + \sum_k S_k M_k \quad [6]$$

or

$$\nabla \cdot (\rho \mathbf{u}) = \nabla \cdot \left( \sum_k D_k^{\text{eff}} \nabla M_k C_k \right) + \sum_k S_k M_k \quad [7]$$

Comparing with Eq. 1, one has

$$S_m = \nabla \cdot \left( \sum_k D_k^{\text{eff}} \nabla M_k C_k \right) + \sum_k S_k M_k \quad [8]$$

In the above equations, the diffusion terms contain contributions from the gas and membrane phases. Assuming the sum of multicomponent gas diffusion terms is equal to zero and separating out the water diffusion term through the membrane phase, one arrives at

$$\begin{aligned} S_m &= M_w \nabla \cdot (D_w^m \nabla C_w^m) + \sum_k S_k M_k \\ &= M_w \nabla \cdot (D_{w,m} \nabla C_w) + \sum_k S_k M_k \end{aligned} \quad [9]$$

where  $C_w^m$  is the molar concentration of water in the membrane phase, and  $D_{w,m}$  is the modified diffusion coefficient for water dif-

**Table II. Source terms for the conservation equations in each region.<sup>8</sup>**

	$S_u$	$S_k$	$S_\phi$	$S_m$
Gas channels	0	0	—	0
Diffusion layers	$-\frac{\mu}{K_{\text{GDL}}}\mathbf{u}$	0	0	0
Catalyst layers	$-\frac{\mu}{K_{\text{CL}}}\mathbf{u}$	$-\nabla \cdot \left(\frac{n_d}{F}i_e\right) - \frac{s_{kj}}{n_k F}$	$j$	$-\sum_k \left(M_k \frac{s_{kj}}{n_k F}\right) - M_w \nabla \cdot \left(\frac{n_d}{F}i_e\right) + M_w(D_{w,m}\nabla C_w)$
Membrane	$-\frac{\mu}{K_m}\mathbf{u}$	0	0	—

Note:

$n_d$  is the electro-osmotic drag coefficient for water. For  $\text{H}_2$  and  $\text{O}_2$ ,  $n_d = 0$ .

fusion through the ionomer if expressed in terms of the gradient in the gas-phase molar concentration with Bruggeman correlation accounting for the tortuosity effect, *i.e.*

$$D_{w,m} = \epsilon_e^{1.5} D_w^m \frac{dC_w^m}{dC_w} \quad [10]$$

In the catalyst layer,  $\epsilon_e$  is the ionomer volume fraction whereas it is unity in the membrane. Note also that there is an electro-osmotic drag term contained in the species source term for  $\text{H}_2\text{O}$ . Thus, physically Eq. 9 indicates that the mass source consists of the consumption or production of species due to electrochemical reactions as well as the water transport fluxes through the membrane due to diffusion and electro-osmotic drag. Details on the water transport model in the membrane have been given in Ref. 8-10, 12 and thus are not repeated here. A similar water transport model through the membrane was also presented by Kulikovskiy.<sup>18</sup>

We choose Eq. 3 to solve for water and oxygen molar concentrations, and then calculate the concentrations of hydrogen and nitrogen by ideal gas law

$$C_{\text{H}_2/\text{N}_2} = \frac{p}{RT} - \sum_{k=\text{others}} C_k \quad [11]$$

This approach of indirectly solving for the hydrogen concentration is valid for a binary gas ( $\text{H}_2/\text{H}_2\text{O}$ ) anode. In this situation, the  $\text{H}_2\text{O}$  species equation along with the ideal gas law (*i.e.*, Eq. 11) provides a sufficient number of equations for two unknowns:  $\text{H}_2$  and  $\text{H}_2\text{O}$  molar concentrations. Note also that hydrogen is strictly conserved in this approach.

The model equations and their physical, transport, and electrochemical properties are summarized in Tables I–III in detail.

It is instructive to estimate the transverse gas velocity induced by the mass source/sink and the ensuing convection effect on species transport. In the one dimension across the GDL and catalyst layer, integration of the continuity equation in the anode results in

$$\rho v = M_{\text{H}_2} \frac{I}{2F} + M_w \alpha \frac{I}{F} = \left(\frac{M_{\text{H}_2}}{2} + M_w \alpha\right) \frac{I}{F} \quad [12]$$

Here,  $v$  is the velocity component in the through-plane direction and  $\alpha$  the net water flux per proton through the membrane, which is a combined effect of electro-osmotic drag and back diffusion. If we define the Peclet number as a parameter to measure the relative strength of this transverse convection to molecular diffusion, it follows that

$$\begin{aligned} Pe &= \frac{v \delta_{\text{GDL}}}{D} = \frac{\left(\frac{M_{\text{H}_2}}{2} + M_w \alpha\right) \frac{I}{F} \delta_{\text{GDL}}}{\rho D} \\ &= 0.03(1 + 18\alpha) \\ &\approx 0.1 \end{aligned} \quad [13]$$

for  $I = 1.0 \text{ A/cm}^2$ ,  $\delta_{\text{GDL}} = 0.3 \text{ mm}$ , and  $\alpha = 0.1$ . This indicates that the convection effect due to transverse flow is small as compared to the diffusive transport.

*Variable-flow vs. constant-flow models.*—Note that the model described above fully couples the mass, momentum, and species equations through various source terms and variable density. The flow

**Table III. Electrochemical properties.<sup>8</sup>**

Description	Anode	Cathode
Transfer current density, $j$ ( $\text{A/m}^2$ )	$ai_{0,a} \left(\frac{C_{\text{H}_2}}{C_{\text{H}_2,\text{ref}}}\right)^{1/2} \left(\frac{\alpha_a + \alpha_c}{RT} F \eta\right)$	$-ai_{0,c} \left(\frac{C_{\text{O}_2}}{C_{\text{O}_2,\text{ref}}}\right) \exp\left(-\frac{\alpha_c F}{RT} \eta\right)$
Surface overpotential, $\eta$ (V)	$\Phi_s - \Phi_e - U_o$ (with $\Phi_s = 0$ )	$\Phi_s - \Phi_e - U_o$ (with $\Phi_s = V_{\text{cell}}$ )
Equilibrium potential, $U_o$ (V)	0	$1.23 - 0.9 \times 10^{-3}(T - 298)$
Exchange current density $\times$ reaction surface area, $ai_0$ ( $\text{A/m}^2$ )	$1.0 \times 10^9$	$10^4$
Transfer coefficient, $\alpha$	$\alpha_a + \alpha_c = 2$	$\alpha_c = 1$

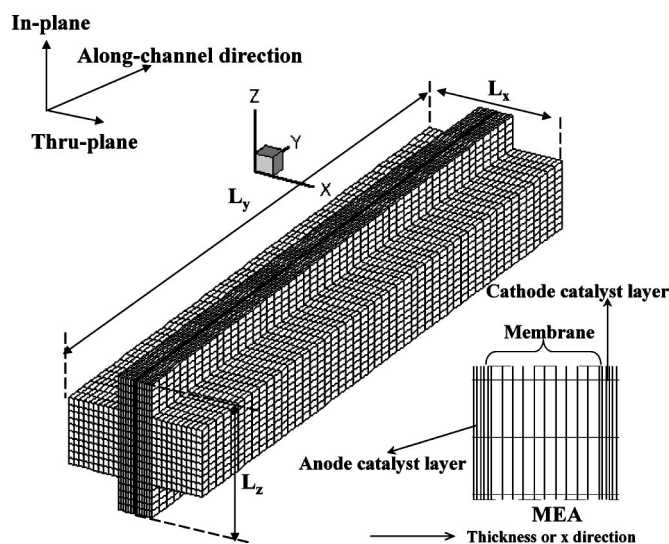


Figure 1. Computational domain and mesh of a single-channel PEFC.

field determined by the mass and momentum equations, Eq. 1 and 2, is strongly affected by the electrochemical processes via the mass source term,  $S_m$ , and variable density. This is hence termed variable-flow model. An elegant simplification of this full model is to neglect the mass source in the continuity equation and assume a constant gas density in the momentum equation. It follows that Eq. 1 and 2 are simplified to

$$\nabla \cdot (\mathbf{u}) = 0 \quad [14]$$

$$\frac{1}{\epsilon^2} \nabla \cdot (\mathbf{u}\mathbf{u}) = -\nabla \frac{p}{\rho} + \nabla \cdot \frac{\boldsymbol{\tau}}{\rho} + \frac{S_u}{\rho} \quad [15]$$

Equation 14 and 15 then yield a flow field that is dependent only on the inlet flow boundary condition and channel geometry, regardless of any electrochemical process occurring in a PEFC. This simplified model, termed the constant-flow model herein, effectively decouples the flow field from the species (with reaction) and potential equations, thereby significantly accelerating calculations and reducing memory requirements. Both models will be compared in the next section to assess possible inaccuracy introduced by the constant-flow model.

Table IV. Geometrical and operating parameters.

Quantity	Value
Gas channel depth/width	1.0/1.0 mm
Shoulder width	1.0 mm
GDL thickness, $\delta_{GDL}$	0.3 mm
Catalyst layer thickness, $\delta_{CL}$	0.01 mm
Membrane (N112) thickness, $\delta_m$	0.051 mm
Fuel cell height/length	2.0/100.0 mm
Anode/cathode inlet pressures, $P$	2.0/2.0 atm
Cathode stoichiometry (stoich <sub>c</sub> ), $\xi_c$ at 0.5 A/cm <sup>2</sup>	2.0
Temperature of fuel cell, $T$	353 K
Relative humidity of anode/cathode inlet	50/0%
Porosity of GDLs, $\epsilon$	0.6
Porosity of catalyst layers, $\epsilon_g$	0.4
Volume fraction of ionomer in catalyst layers, $\epsilon_m$	0.26
Permeability of diffusion layers, $K_{GDL}$	$10^{-12}$ m <sup>2</sup>
Permeability of catalyst layers, $K_{CL}$	$10^{-15}$ m <sup>2</sup>

Table V. Comparison of the results between the two models.

	Stoich <sub>a</sub> = 1.2	Stoich <sub>a</sub> = 2.0
C flow model	0.50 A/cm <sup>2</sup> at 0.595 V	0.41 A/cm <sup>2</sup> at 0.625 V
V flow model	0.50 A/cm <sup>2</sup> at 0.610 V	0.45 A/cm <sup>2</sup> at 0.625 V

**Boundary conditions.**—Seven unknowns:  $\mathbf{u}$ ,  $P$ ,  $C_{O_2}$ ,  $C_w$ , and  $\phi_e$  are involved in the coupled differential governing equations, Eq. 1 through 4, that require boundary conditions.

**Flow inlets.**—The inlet velocity  $\mathbf{u}_{in}$  in a gas channel is expressed by the respective stoichiometric flow ratio, *i.e.*,  $\xi_a$  or  $\xi_c$ , defined at the reference current density,  $I_{ref}$ , as

$$\xi_a = \frac{C_{H_2}^a u_{in,a} A_a}{I_{ref} A} \quad \text{and} \quad \xi_c = \frac{C_{O_2}^c u_{in,c} A_c}{I_{ref} A} \quad [16]$$

where  $A_a$  and  $A_c$  are the flow cross-sectional areas of the anode and cathode gas channels, respectively and  $u_{in,a}$  and  $u_{in,c}$  the inlet velocities of the channels. The inlet molar concentrations,  $C_k^a$  and  $C_k^c$ , are determined by the inlet pressure and humidity according to the ideal gas law.

**Outlets.**—Fully developed or no-flux conditions are applied

$$\frac{\partial \mathbf{u}}{\partial n} = 0, \quad \frac{\partial C_k}{\partial n} = 0, \quad \frac{\partial \phi_e}{\partial n} = 0 \quad [17]$$

**Walls.**—No-slip and impermeable velocity condition and no-flux conditions are applied

$$\mathbf{u} = 0, \quad \frac{\partial C_k}{\partial n} = 0, \quad \frac{\partial P}{\partial n} = 0, \quad \frac{\partial \phi_e}{\partial n} = 0 \quad [18]$$

**Numerical procedures.**—The governing equations are solved by the commercial CFD software package, Fluent (version 6.0.12), with SIMPLE (semi-implicit pressure linked equation) algorithm.<sup>20</sup> The source terms and physical properties are incorporated into a UDF (user-defined functions), based on the software's user-coding capability.<sup>21</sup> The mesh of a single-channel PEFC employed in this work is shown in Fig. 1 with the anode and cathode in coflow. Geometrical and operating parameters of this PEFC are listed in Table IV. About 100,000 ( $51 \times 100 \times 20$ ) computational cells are used to capture the complex electrochemical and physical phenomena in the PEFC. In addition, overall species mass balance is checked besides the equation residuals as important convergence criteria. These species balance checks also ensure physically meaningful results to be obtained. In all the simulations presented in the next section, values of species mass imbalance (*i.e.*,  $H_2$ ,  $O_2$ , and  $H_2O$ ) are all less than 0.1%.

## Results and Discussion

Two limiting conditions representative of common PEFC operation, *i.e.*, anode stoichiometry of 1.2 and 2.0, were chosen to display detailed calculation results with the cathode stoichiometry fixed at 2.0. Other operating conditions are listed in Table IV. Particularly, we are interested in exploring the low-humidity operation (*i.e.*,  $RH_a/RH_c = 50\%/0\%$ ), where water transport characteristics in the anode may be altered by variable flow under large density and velocity changes, thereby affecting the cell performance. Table V lists two comparisons between the two models: one is at the anode stoichiometry of 2.0 at 0.5 A/cm<sup>2</sup> and under a constant cell voltage of 0.625 V, and the other is at the anode stoichiometry of 1.2 and under a constant current density of 0.5 A/cm<sup>2</sup>.

Figure 2 displays the axial profiles of the mass source in the anode catalyst layer, scaled by the anode inlet flow rate. The total mass source consists of the contributions from hydrogen consump-

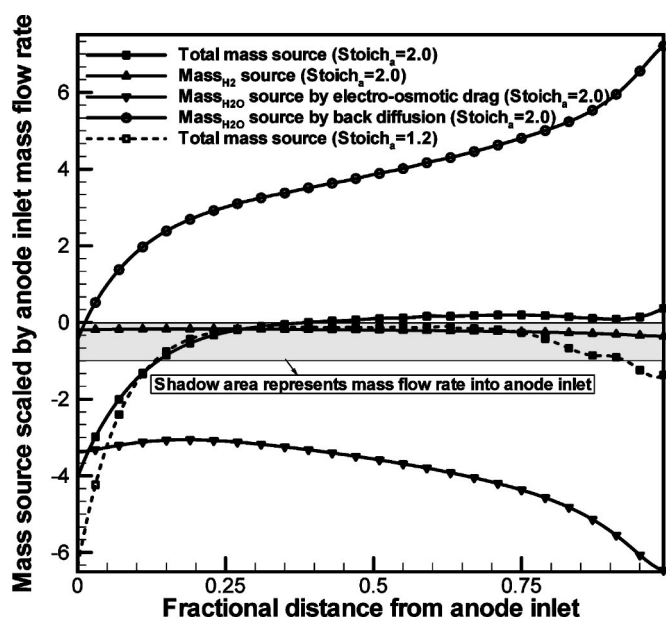


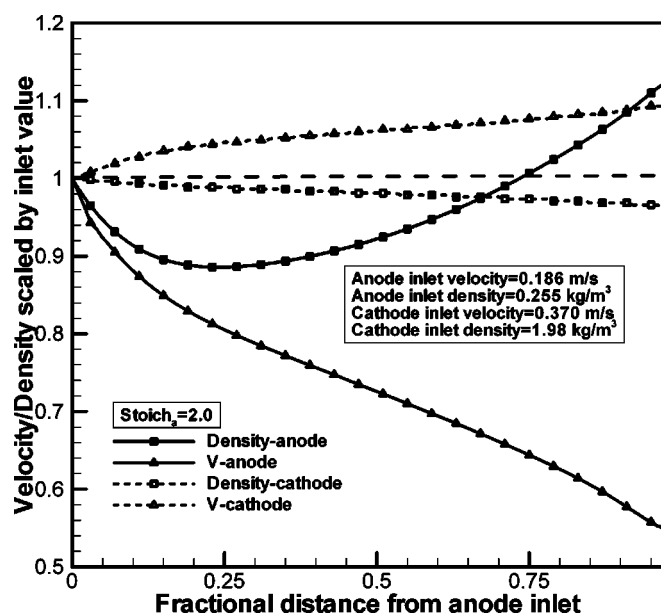
**Figure 2.** Mass sources in the anode catalyst layer scaled by the mass injection rate in anode predicted by the variable-flow model for  $\text{stoich}_a = 2.0$  (at 0.625 V and 0.45 A/cm<sup>2</sup>) and 1.2 (at 0.61 V and 0.5 A/cm<sup>2</sup>), respectively.

tion, water electro-osmotic drag, and water back diffusion. The integral of each curve represents the ratio of the total mass source/sink in the catalyst layer to the anode inlet flow rate. For  $\text{stoich}_a = 2.0$ , the anode loses a large amount of mass in the first quarter of the channel due to water electro-osmotic drag across the membrane, and gradually gets mass back from back diffusion of water in the latter part of the fuel cell. Compared with the mass source due to water, hydrogen contribution is negligibly small. In addition, it can be seen in Fig. 2 that the two water sources due to electro-osmotic drag and diffusion, respectively, almost cancel each other starting from the dimensionless distance of 25% into the channel, making the total mass source small in the last three-quarters of the channel. In  $\text{stoich}_a = 1.2$ , it can be seen from Fig. 2 that the anode always loses mass to the cathode and magnitude of the total mass source is significant not only in the first quarter but also the last quarter of the channel.

Figure 3 shows streamwise variations of the average axial velocity and density in gas channels predicted by the variable-flow model for  $\text{stoich}_a = 2.0$ . The density in the cathode decreases only by 4% along the channel, while that in the anode decreases by 12% over the first quarter of the length, then increases back by  $\sim 30\%$  from the lowest density. The negligible variation in the cathode gas density is expected as nitrogen is a diluent of dominant composition. The large density variation in the anode stems from the large density contrast of hydrogen to water vapor. In addition to the density change, the velocity variation along the fuel cell length is more dramatic. Figure 3 shows that the anode average velocity decreases by nearly 50%, while the cathode velocity changes by 9%. Again, the small variation in the cathode velocity may be explained by the much larger density of the cathode gas stream.

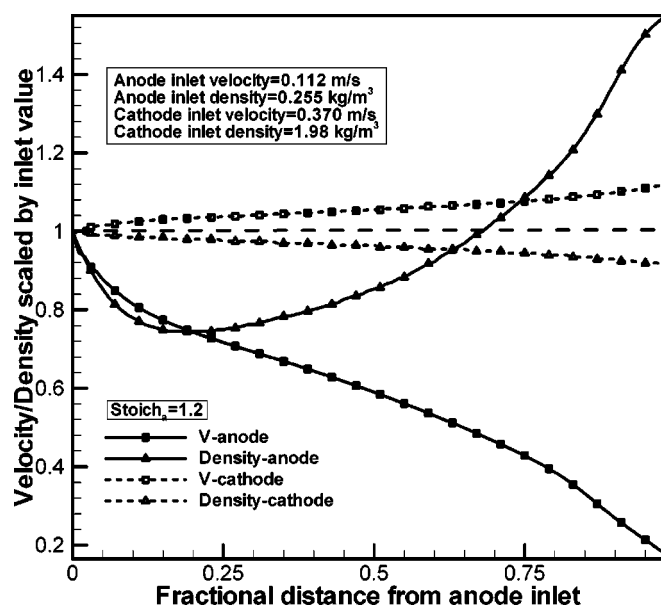
Figure 4 shows the same density and velocity profiles for  $\text{stoich}_a = 1.2$ . Now, the density and velocity changes become much more severe due to the much smaller anode flow rate, amounting to greater than 50 and 80%, respectively. As a result of the large change in the axial velocity, species transport in the anode channel dominated by convection may be quite different from that in a constant flow.

Figure 5 compares the average water/hydrogen molar concentrations along the anode gas channel for  $\text{stoich}_a = 2.0$ , between the



**Figure 3.** Average axial velocity and density in gas channels predicted by the variable-flow model for  $\text{stoich}_a = 2.0$  and 0.625 V.

variable-flow and constant-flow models. The most remarkable difference is in the hydrogen concentration profile. The variable-flow model predicts an almost flat profile and H<sub>2</sub> molar concentration retains about the inlet value. In contrast, the constant-flow model predicts a sharply declined H<sub>2</sub> profile. This is because in the constant-flow model, the flow rate does not decrease as in the variable-flow model and consequently the concentration must be lowered to satisfy hydrogen consumption by the anode reaction. This dramatic difference in hydrogen concentration, however, does not impact the overpotential for hydrogen oxidation reaction (HOR) as the reaction is sufficiently facile under both concentrations. As compared with hydrogen, the water concentration profiles predicted by both models are much closer. They look similar also in that the water concentration decreases near the inlet due to dominance of



**Figure 4.** Average axial velocity and density in gas channels predicted by the variable-flow model for  $\text{stoich}_a = 1.2$  and 0.5 A/cm<sup>2</sup>.

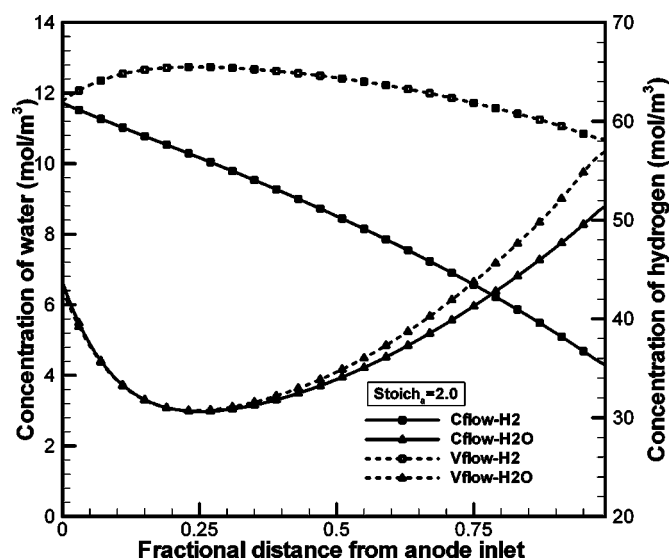
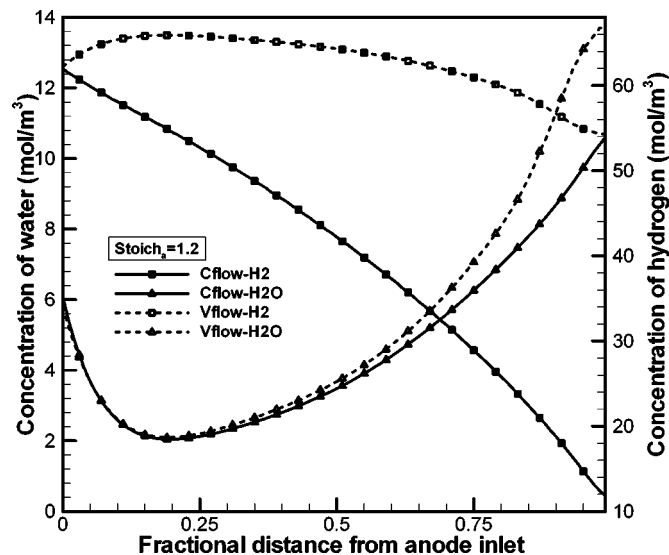


**Figure 5.** Comparison of average water/hydrogen molar concentrations in the anode gas channel between the constant-flow and variable-flow models for  $\text{stoich}_a = 2.0$  and  $0.625$  V.

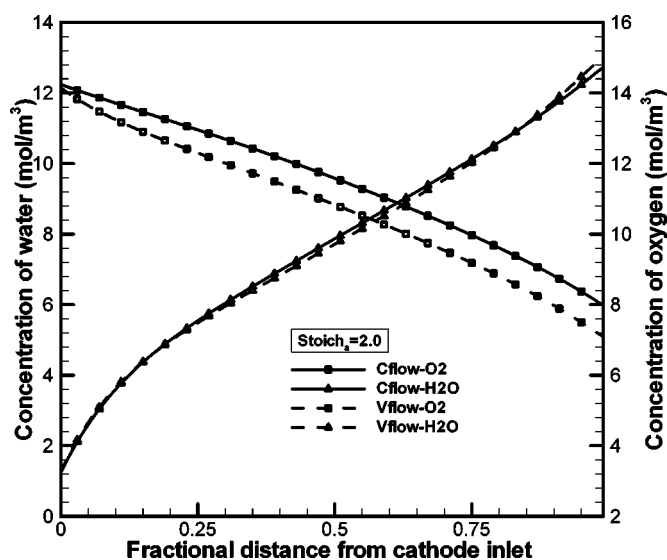
electro-osmotic drag and then increases due to enhanced back diffusion. Figure 6 compares similar profiles for  $\text{stoich}_a = 1.2$ . The same trends discussed above prevail except that the differences between the two models are enlarged, as expected.

Figure 7 presents water/oxygen molar concentrations averaged in the cathode gas channel for  $\text{stoich}_a = 2.0$ . Compared with Fig. 5, differences on the cathode side between the two models are much smaller due largely to the lesser variation in density and axial velocity in the cathode as shown in Fig. 3. Interestingly, the water distributions are almost identical whereas there is little difference in the oxygen profiles between the two models. Note that the average current densities in this comparison for  $\text{stoich}_a = 2.0$  under constant cell voltage of  $0.625$  V are slightly different:  $0.41$  and  $0.45$  A/cm<sup>2</sup> from the constant-flow and variable-flow models, respectively.

Details of the transverse flow in the fuel cell cross section are shown in Fig. 8 through 10 for three representative axial locations:



**Figure 6.** Comparison of average water/hydrogen molar concentrations in the anode gas channel between the constant-flow and variable-flow models for  $\text{stoich}_a = 1.2$  and  $0.5$  A/cm<sup>2</sup>.



**Figure 7.** Comparison of average water/oxygen molar concentrations in the cathode gas channel between the constant-flow and variable-flow models for  $\text{stoich}_a = 2.0$  and  $0.625$  V.

the inlet, the middle, and the outlet. In each figure, the velocity vectors are presented for  $\text{stoich}_a = 2.0$  along with contours of a scalar as predicted by the variable-flow model. First, near the anode inlet, there is a strong transverse flow going from the anode to

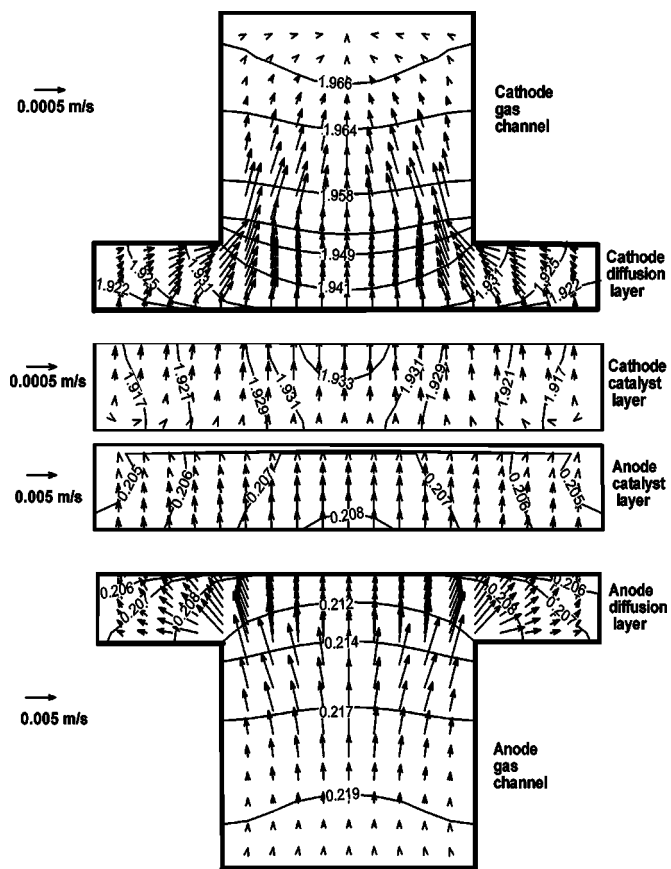


**Figure 8.** Distributions of velocity and density in the cross section near the inlet (*i.e.*,  $y = L_y/20$ ), predicted by the variable-flow model for  $\text{stoich}_a = 2.0$  and  $0.625$  V. The catalyst layers are expanded for clarity.

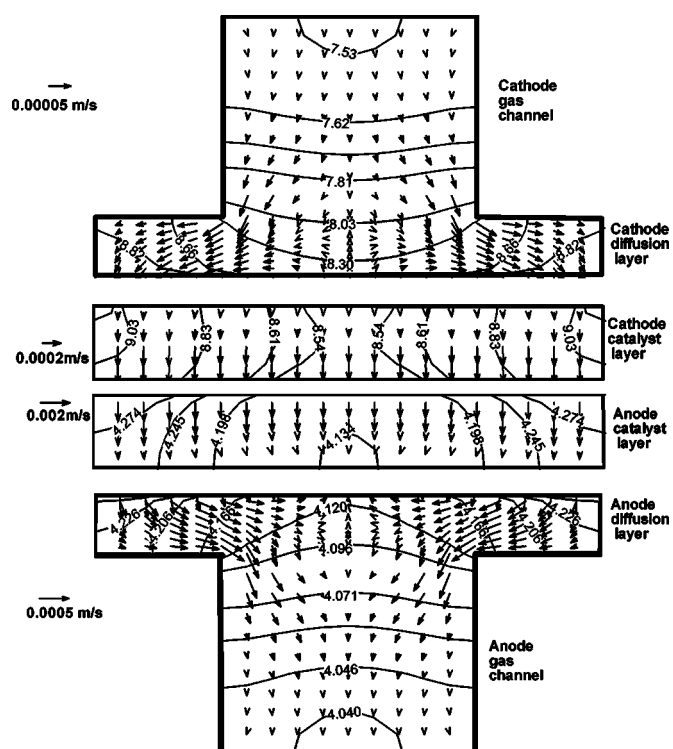


**Figure 9.** Distributions of the velocity and water concentration in the cross section at midlength of the PEFC (*i.e.*,  $y = L_y/2$ ), predicted by the variable-flow model for  $\text{stoich}_a = 2.0$  and 0.625 V. The catalyst layers are expanded for clarity.

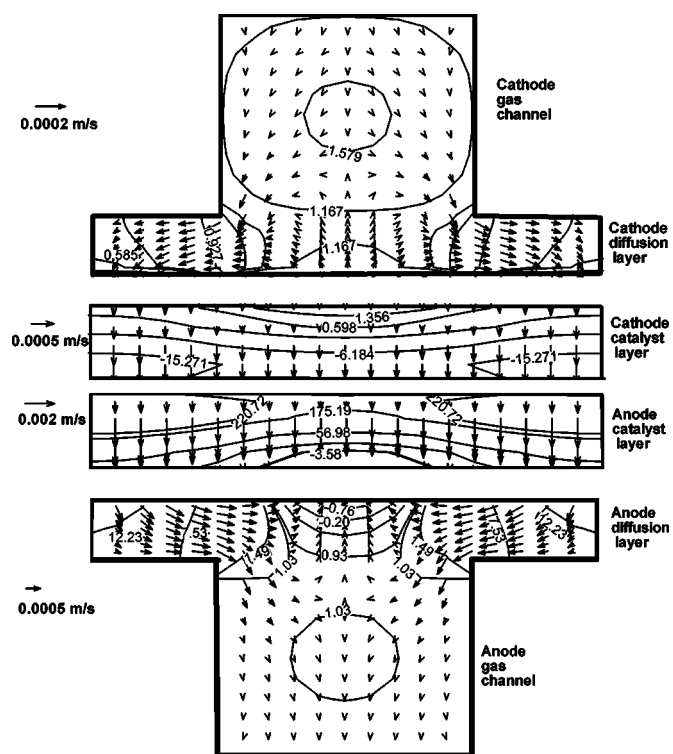


**Figure 10.** Distributions of the velocity and pressure in the cross section near the outlet (*i.e.*,  $y = (19/20)L_y$ ), predicted by the variable-flow model for  $\text{stoich}_a = 2.0$  and 0.625 V. The catalyst layers are expanded for clarity.

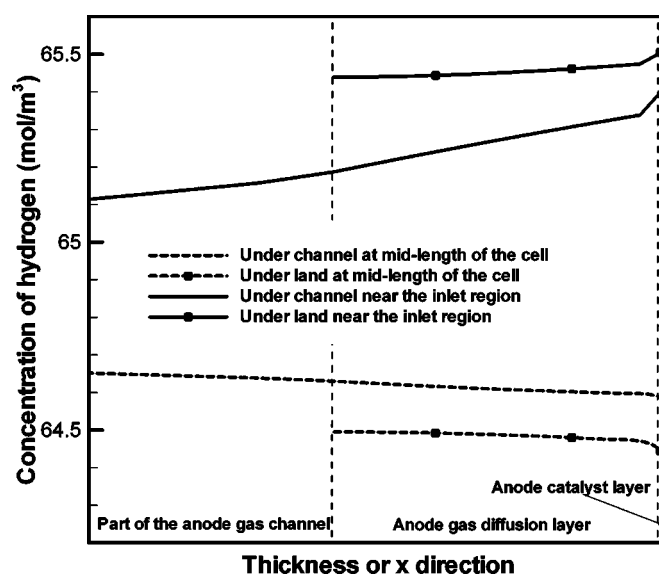


**Figure 11.** Profiles of hydrogen concentrations in the through-plane direction in the anode for  $\text{stoich}_a = 2.0$  and 0.625 V, predicted by the variable-flow model.

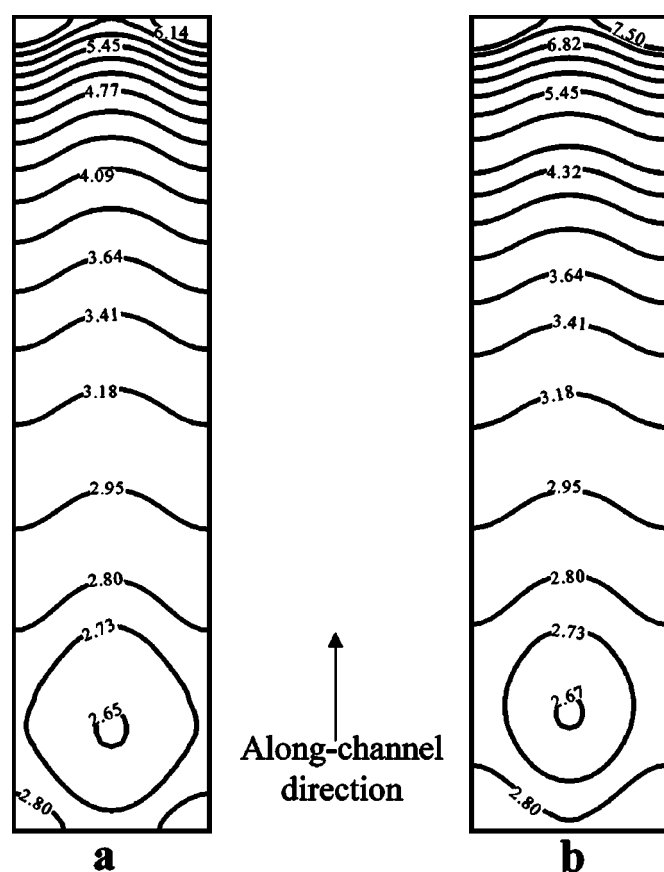
cathode, as shown in Fig. 8. In the anode GDL, the magnitude of the velocity is about 0.005 m/s, and hence the Peclet number,  $v \delta_{\text{GDL}}/D$ , of  $\sim 0.15$ . This is consistent with the estimate presented in Eq. 13 and indicates that diffusive transport of species dominates in the GDL. Figure 8 also shows the cross-sectional density distribution and indicates that the density is smaller in the anode catalyst layer as a result of the lower water concentration due to electro-osmotic drag. In addition, density variation in the through-plane direction is within 7%. On the cathode side, Fig. 8 shows that the transverse velocity is nearly ten times smaller than that in the anode. Thus, the convection effect in the cathode GDL can be safely ignored. In addition, the density variation in the cathode is less than 2%.

Figure 9 shows the cross-sectional velocity vectors and water concentration contours at the midlength of the cell. At this location, strong back diffusion of water occurs, as evident from the higher water concentration on the cathode side. The back diffusion then offsets the electro-osmotic drag, thus leading to a much smaller transverse flow than in Fig. 8.

Figure 10 shows the cross-sectional velocity vectors and pressure contours in the outlet region. This location also features strong back diffusion of water, thus yielding a transverse flow pattern similar to Fig. 9. In addition, because there is flow in the porous media, there exist pressure variations in GDLs and catalyst layers. The maximum pressure drop across the GDL and catalyst layer is around 12 and 220 Pa, respectively, in comparison to the operating pressure of  $2 \times 10^5$  Pa.

Another observation from Fig. 10 is that there exists a pressure difference between the two surfaces of the membrane, even though the gas stream pressures are equal on the two sides. While depending on the permeability of the catalyst layer, a pressure difference of 220 Pa is possible as presented in Fig. 10.

Figure 11 shows the profiles of hydrogen concentration in the through-plane direction for  $\text{stoich}_a = 2.0$  near the inlet and at the midlength of the cell. Only part of the gas channel is included to show more details in the porous GDL and catalyst layer. At the midlength of the cell, both curves under the land and channel exhibit a decline from the GDL toward the catalyst layer, indicative of a diffusion-reaction process. In addition, there is lower hydrogen concentration under the land than the channel due to the land blockage on species transport. However, near the inlet region, both curves under the land and channel reveal a totally opposite trend: hydrogen concentration increases from the channel, to the GDL, and to the



**Figure 12.** Comparison of the water content distributions in the middle membrane between the (a) constant-flow and (b) variable-flow models for  $\text{stoich}_a = 2.0$  and  $0.625$  V.

catalyst layer, while the concentration under the land is higher than under the channel. The reverse profile results clearly from the strong transverse flow existing in the region. Nonetheless, the weak effect of convection leads only to a very slight increase in the  $\text{H}_2$  concentration.

Figure 12 presents contours of water content in the middle membrane for  $\text{stoich}_a = 2.0$ , which determines the ionic resistance of the fuel cell. Here water content is defined as the number of water molecules per sulfonic group in the membrane. The distributions from the two models are similar in most parts of the membrane. A difference appears in the outlet region, where higher water content is indicated for the variable-flow model, which is ascribed to the higher water concentration in the anode channel as shown in Fig. 5. In addition, near the inlet area, water content predicted by the variable-flow model is a little higher, which can be explained by convection induced by the transverse flow in the anode GDL as shown in Fig. 8.

The distributions of local current density from the two models are compared in Fig. 13, showing that the current density contours are again similar for the most part. Similar to Fig. 12, differences arise in the outlet and inlet regions. The difference in the average current density between the two models is less than 10% for  $\text{stoich}_a = 2.0$  and  $0.625$  V.

Using the polarization curve as a figure of merit, Fig. 14 attempts to establish the validity range of the constant-flow model. First, a comparison is made in Fig. 14 between the two models for  $\text{stoich}_a = 2.0$  at  $0.5 \text{ A/cm}^2$  and full humidification of both anode and cathode. No appreciable difference is observed, demonstrating that the constant-flow model is a physically sound and computationally advantageous model for PEFCs operated under high to full humidification. For low-humidity operation (e.g.,  $\text{RH}_{a/c} = 50\%/0\%$ ), we ex-

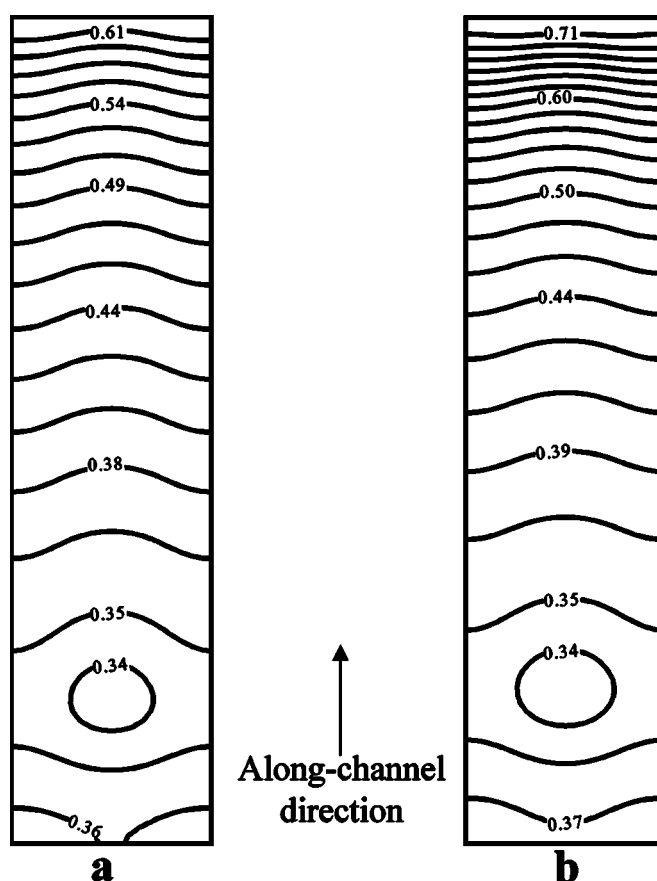


**Figure 13.** Comparison of current density distributions between the (a) constant-flow and (b) variable-flow models for  $\text{stoich}_a = 2.0$  and  $0.625$  V.

amined the anode stoichiometric ratios of 1.2 and 2.0. As seen from Fig. 14, the differences in the average current density are less than 14 and 10% for the anode stoichiometry of 1.2 and 2.0, respectively. Note also that the two polarization curves at  $\text{stoich}_a = 1.2$  are ter-

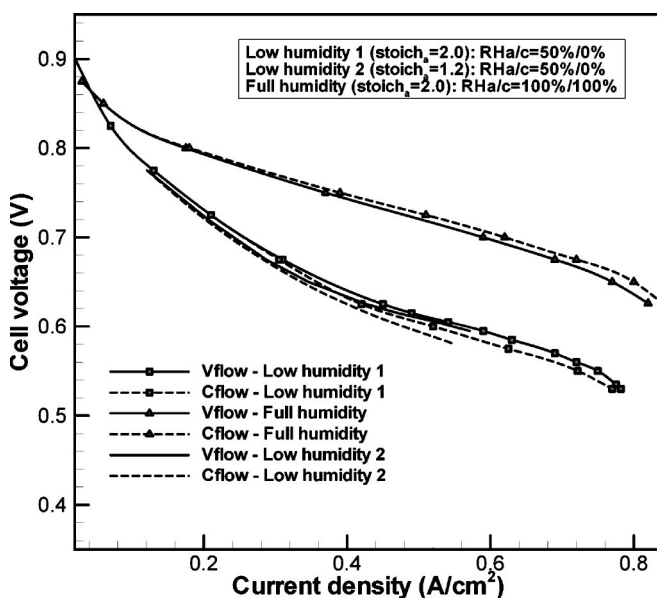


**Figure 14.** Comparison of polarization curves for the two models.

minated before 0.6 A/cm<sup>2</sup> which is the maximum current density possible for H<sub>2</sub> stoichiometry of 1.2 at 0.5 A/cm<sup>2</sup>.

### Conclusions

A three-dimensional, multicomponent model of PEFCs has been developed to fully couple the flow field with transport and electrochemical processes, with focus on studying operation with very large density and velocity variations. Numerical simulations were carried out for a single-channel PEFC operated under common conditions with the anode stoichiometry setting to 1.2 and 2.0, respectively, and the results were compared with the previous constant-flow model. Simulation results indicate that the density and velocity along the anode channel may change by more than 50 and 80%, respectively. Deceleration of the anode gas flow under low anode stoichiometry is a major finding from the present full model. As a result of anode flow deceleration, the hydrogen concentration remains high. Despite all these dramatic differences in the anode density, flow, and H<sub>2</sub> concentration, the variable-flow and constant-flow models yield similar water and current distributions for anode stoichiometry as low as 1.2. The error in the average current density predicted by the constant-flow model is less than 10 and 14% for the anode stoichiometry of 2.0 and 1.2, respectively, thus supporting the applicability of the constant-flow model under common PEFC operation. Selective contours of density, pressure, and water concentration were also provided to illustrate the fundamental flow and transport processes occurring in PEFCs undergoing large density and velocity changes.

### Acknowledgments

Support for this work by the U.S. Department of Energy and ConocoPhillips under cooperative agreement DE-FC26-01NT41098, and by Honda R&D Co. Ltd is gratefully acknowledged.

The Pennsylvania State University assisted in meeting the publication costs of this article.

### List of Symbols

<i>A</i>	superficial electrode area, m <sup>2</sup>
<i>a</i>	water activity; effective catalyst area per unit volume, m <sup>2</sup> /m <sup>3</sup>
<i>C<sub>k</sub></i>	molar concentration of species <i>k</i> , mol/m <sup>3</sup>
<i>D</i>	mass diffusivity of species, m <sup>2</sup> /s
EW	equivalent weight of dry membrane, kg/mol
<i>F</i>	Faraday's constant, 96,487 C/equiv
<i>I</i>	current density, A/cm <sup>2</sup>
<i>i<sub>e</sub></i>	superficial current density, A/m <sup>2</sup>
<i>j</i>	transfer current, A/cm <sup>3</sup>
<i>K</i>	permeability, m <sup>2</sup>
<i>L</i>	length, m
<i>M</i>	molecular weight, kg/mol
<i>n</i>	unit vector normal to a surface
<i>n<sub>d</sub></i>	electro-osmosis coefficient, H <sub>2</sub> O/H <sup>+</sup>
<i>P</i>	pressure, Pa
<i>Pe</i>	Peclet number
<i>R</i>	universal gas constant, 8.134 J/mol K
<i>S</i>	source term
<i>s</i>	stoichiometry coefficient in electrochemical reaction
<i>t</i>	time, s
<i>T</i>	temperature, K
<i>U<sub>o</sub></i>	equilibrium potential, V
<i>u</i>	velocity vector, m/s

<i>V<sub>cell</sub></i>	cell potential, V
<i>X</i>	mole fraction

### Greek

$\alpha$	transfer coefficient; net water flux per proton flux
$\delta$	thickness, m
$\epsilon$	porosity
$\eta$	surface overpotential, V
$\kappa$	ionic conductivity, S/m
$\lambda$	membrane water content
$\mu$	viscosity, kg/m s
$\xi$	stoichiometric flow ratio
$\rho$	density, kg/m <sup>3</sup>
$\tau$	shear stress, N/m <sup>2</sup>
$\phi$	phase potential, V

### Superscripts and Subscripts

<i>a</i>	anode
<i>c</i>	cathode
CL	catalyst layer
<i>e</i>	electrolyte
eff	effective value
<i>g</i>	gas phase
GDL	gas-diffusion layer
in	inlet
<i>k</i>	species
<i>m</i>	membrane phase
<i>o</i>	gas channel inlet value; reference value
ref	reference value
sat	saturate value
<i>w</i>	water

### References

1. C. Y. Wang, *Chem. Rev. (Washington, D.C.)*, **104**, 4727 (2004).
2. D. M. Bernardi and M. W. Verbrugge, *J. Electrochem. Soc.*, **139**, 2477 (1992).
3. T. E. Springer, T. A. Zawodzinski, and S. Gottesfeld, *J. Electrochem. Soc.*, **138**, 2334 (1991).
4. T. E. Springer, M. S. Wilson, and S. Gottesfeld, *J. Electrochem. Soc.*, **140**, 3513 (1993).
5. T. F. Fuller and J. Newman, *J. Electrochem. Soc.*, **140**, 1218 (1993).
6. T. V. Nguyen and R. E. White, *J. Electrochem. Soc.*, **140**, 2178 (1993).
7. V. Garau, H. Liu, and S. Kakac, *AIChE J.*, **44**, 2410 (1998).
8. S. Um, C. Y. Wang, and K. S. Chen, *J. Electrochem. Soc.*, **147**, 4485 (2000).
9. S. Um and C. Y. Wang, in *Proceedings of the ASME IMECE*, Orlando, FL, Vol. 1, p. 19 (2000).
10. S. Um and C. Y. Wang, *J. Power Sources*, **125**, 40 (2004).
11. H. Meng and C. Y. Wang, *J. Electrochem. Soc.*, **151**, A358 (2004).
12. S. Um, Ph.D. Thesis, The Pennsylvania State University, University Park, PA (2002).
13. H. Meng and C. Y. Wang, *Chem. Eng. Sci.*, **59**, 3331 (2004).
14. Y. Wang and C. Y. Wang, *J. Power Sources*, Submitted.
15. S. Dutta, S. Shimpalee, and J. W. Van Zee, *Int. J. Heat Mass Transfer*, **44**, 2029 (2001).
16. S. Dutta, S. Shimpalee, and J. W. Van Zee, *J. Appl. Electrochem.*, **30**, 135 (2000).
17. F. Büchi and G. G. Scherer, *J. Electrochem. Soc.*, **148**, A183 (2001).
18. A. A. Kulikovskiy, *J. Electrochem. Soc.*, **150**, A1432 (2003).
19. Y. Wang and C. Y. Wang, *Electrochim. Acta*, **50**, 1307 (2005).
20. S. V. Patankar, *Numerical Heat Transfer and Fluid Flow*, Hemisphere Publishing Corp., New York (1980).
21. Fluent 6.1 UDF Manual, Fluent Inc. (2003).
22. S. Motupally, A. J. Becker, and J. W. Weidner, *J. Electrochem. Soc.*, **147**, 3171 (2000).
23. T. A. Zawodzinski, J. Davey, J. Valerio, and S. Gottesfeld, *Electrochim. Acta*, **40**, 297 (1995).
24. A. C. West and T. F. Fuller, *J. Appl. Electrochem.*, **26**, 557 (1996).
25. R. B. Bird, W. E. Stewart, and E. N. Lightfoot, *Transport Phenomena*, John Wiley & Sons, New York (1960).
26. F. P. Incropera and D. P. DeWitt, *Fundamentals of Heat and Mass Transfer*, John Wiley & Sons, New York (1996).